HIGH PERFORMANCE COMPUTING OF KELVIN-HELMHOLTZ INSTABILITY

SAM SKILLMAN[†], SCOTT RECKINGER[§], SHANON RECKINGER[§]

1. Introduction

The Kelvin-Helmholtz instability is a stratified shear instability. The instability occurs in many applications and specifically occurs naturally in the ocean and atmosphere when a velocity shear is present in the flow. In the ocean and atmosphere, this instability is also one of the primary sources of small-scale vertical mixing. This paper investigates the wind shear processes that occur spontaneously under stably stratified conditions. These processes are currently poorly parameterized. Unfortunately, it has been found the global ocean circulation models have a strong sensitivity to the magnitude of the parameterized small-scale vertical mixing ([3]). This is also true in the atmosphere. Therefore, understanding how the dynamics of the Kelvin-Helmholtz instability is important for the scientific community. Figure 1 shows an example of what this instability looks like in the atmosphere.

Figure 1. A photo of Kelvin-Helmholtz instability in the real world. (http://en.wikipedia.org/wiki/File:Wavecloudsduval.jpg)

2. Problem Setup

In this study, various cases are run and compared to further explore the dynamics of this instability. These are all done at a Richardson number of 0.20 and a Reynolds number of 2300. The non-dimensional governing equations are,

$$\partial_t \vec{u} + \vec{u} \cdot \nabla \vec{u} = -\nabla \Pi + Ri\theta\hat{z} + Re^{-1}\nabla^2\vec{u}$$

$$\partial_t \vec{\theta} + \vec{u} \cdot \nabla \vec{\theta} = -w + Pe^{-1}\nabla^2\vec{u}$$

$$\nabla \cdot \vec{u} = 0$$

$$Pr = \frac{\nu}{\kappa} = \frac{Pe}{Re}$$

$$Ri = \frac{g\alpha\beta h^2}{U_0^2}$$

$$Re = \frac{U_0 h}{\nu}$$

$$Pe = \frac{U_0 h}{\kappa}$$

These equations are the Navier-Stokes equations with a Boussinesq approximation. Initially, velocity has a shearing profile and temperature has a linear profile (which results in a stably stratified fluid). Figure 2 shows these two profiles.

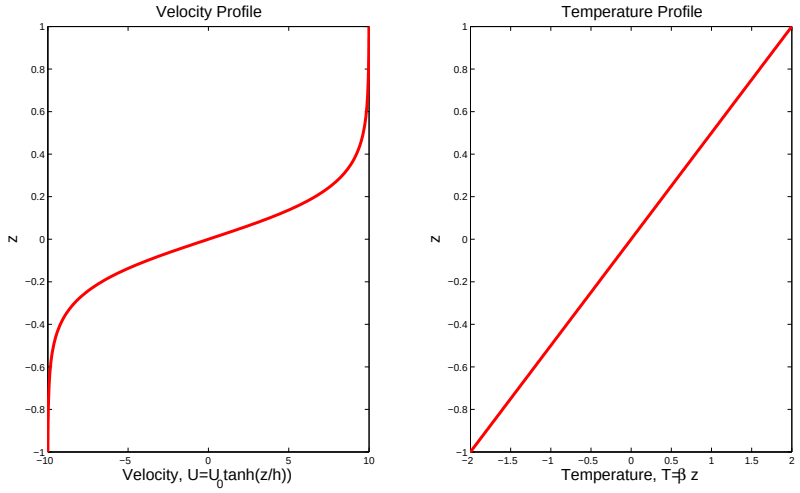

FIGURE 2. Velocity and temperature profiles.

3. Numerical Details

The equations described above are solved using a spectral code, TRIPLE, which uses a spectral algorithm and a real FFT to transform between physical and spectral space. The same system is solved in three ways: 2D Direct Numerical Simulation (DNS), 3D DNS and 3D Large Eddy Simulation (LES). The resolution for these runs are 400×400, $720 \times 180 \times 720$ and $144 \times 36 \times 144$, respectively. They are run to a final non-dimensional time of about 1600, 200 and 250 in units of $\frac{h}{U}$, respectively. The code is run on geppetto.lasp.colorado.edu, a 243-node, 1458-core Sicortex energy-efficient high-performance supercomputer.

DNS refers to performing simulations by attempting to resolve all physical scales of the system. Any numerical method (finite differences, finite elements, etc.) is used without utilizing any models. This high fidelity model is very expensive and not usually ideal for large turbulence problems, such as this atmospheric flow.

LES attempts to solve the issue of the high cost of resolving all the relevant length scales in a problem. It works by applying a spatial filter to eliminate small scales and then accounts for those scales through a turbulence model. This turbulence model needs to supply the correct energy flux at the filter cutoff in order to balance production and dissipation. There are various turbulence models that have been developed including Smagorinsky model, heat flux model, turbulent kinetic energy based model, dynamic models, and many more. The simple eddy viscosity models can achieve the necessary balance, however, need to be carefully calibrated. The dynamic modeling self-calibrates

but requires the filter cutoff to be in the inertial range. The LES approach has been proven successful when the appropriate resolution is used.

4. Results and Discussion

Processing and analysis of the data is performed using multiple software packages. Of particular importance is the use of Vapor([1, 2]), a volume rendering visualization package that utilizes wavelets for display refinement. In this report, the two extremes for the volume rendered plots created from Vapor are red (low values) and violet (high values). For each case, the results from three time steps are presented. The intermediate time is chosen to be when global kinetic energy is maximum throughout the entire growth of the instability. The early time is before peak energy when the global kinetic energy value is half of the maximum value. The late time is after peak energy at a similar global kinetic energy value.

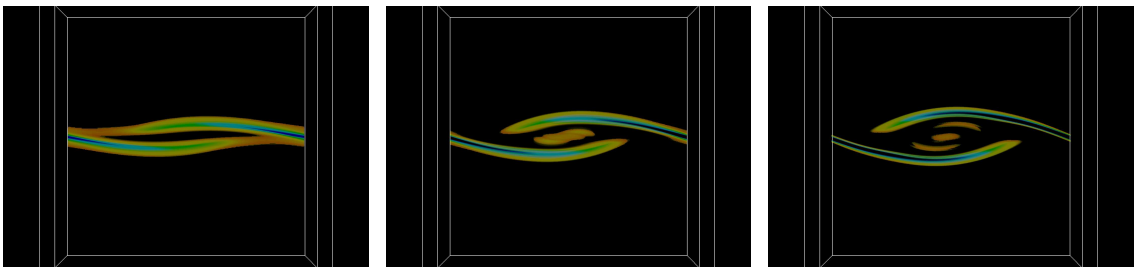

(a) time=55 (b) time=90 (c) time=135

Figure 3. Plots of enstrophy for 2D DNS at three different snapshots in time.

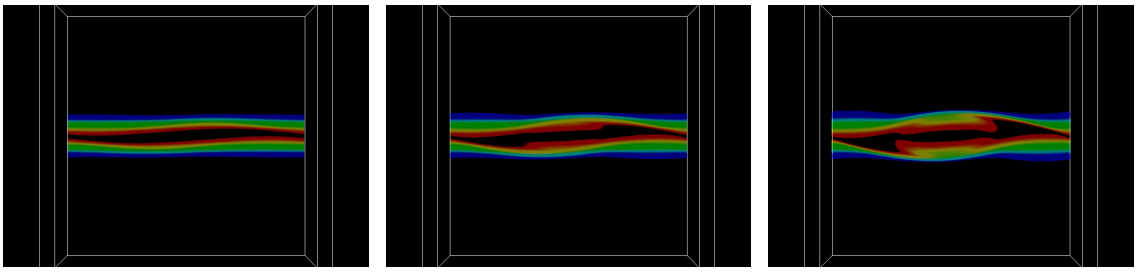

(a) time=55 (b) time=90 (c) time=135

Figure 4. Plots of kinetic energy for 2D DNS at three different snapshots in time.

4.1. **2D DNS.** The 2D DNS case is characterized by the development of a billow. The billow remains laminar and decays slowly. The evolution of enstrophy displayed in Figure 3 shows the billow structure. Kinetic energy and temperature, presented in Figures 4 and 5 respectively, show the lack of mixing in this two-dimensional system. Figure 6 is the y-vorticity, which is simply the square root of enstrophy since the other components of vorticity are zero in a two-dimensional system. The 2D DNS case fails to show any signs of turbulence. The structures in the flow develop and dissipate over a relatively long time scale due to the lack of mixing and the two-dimensional nature of the flow.

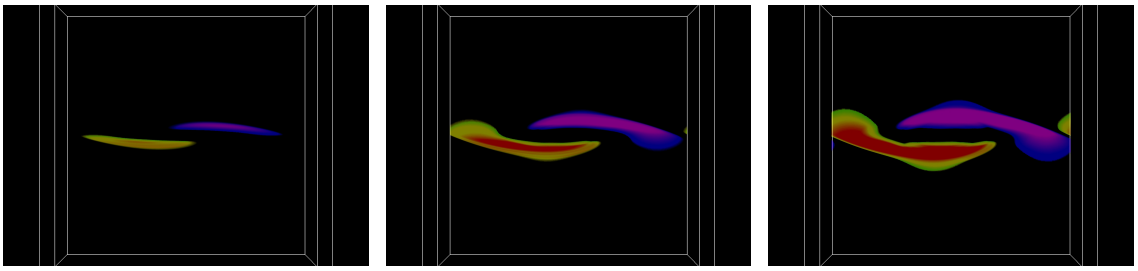

(a) time=55 (b) time=90 (c) time=135

FIGURE 5. Plots of temperature for 2D DNS at three different snapshots in time.

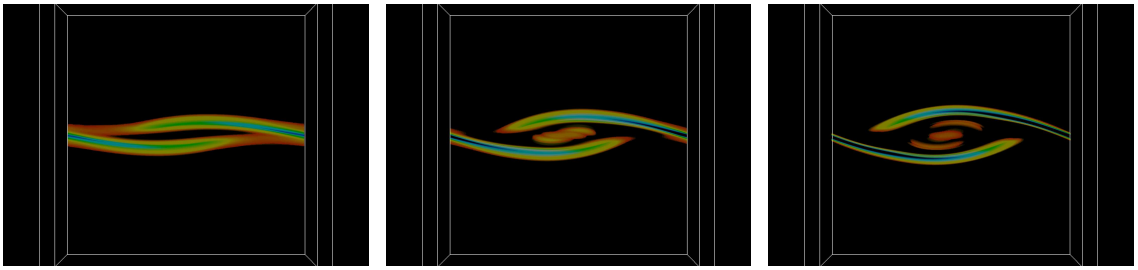

(a) time=55 (b) time=90 (c) time=135

FIGURE 6. Plots of the y component of vorticity for 2D DNS at three different snapshots in time.

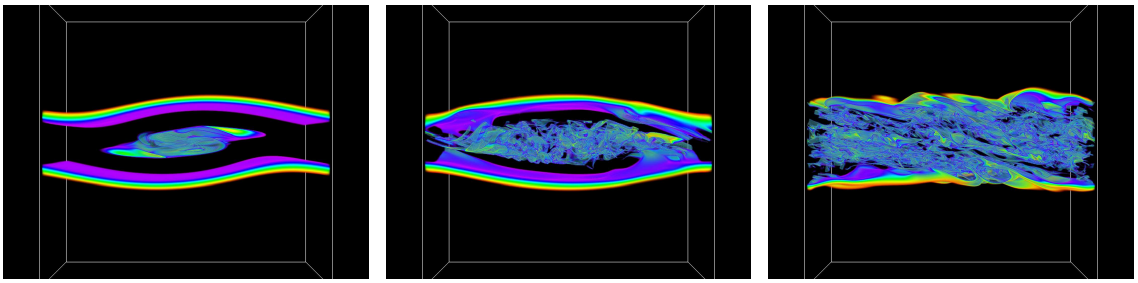

(a) time=55 (b) time=80 (c) time=105

FIGURE 7. Plots of enstrophy for 3D DNS at three different snapshots in time.

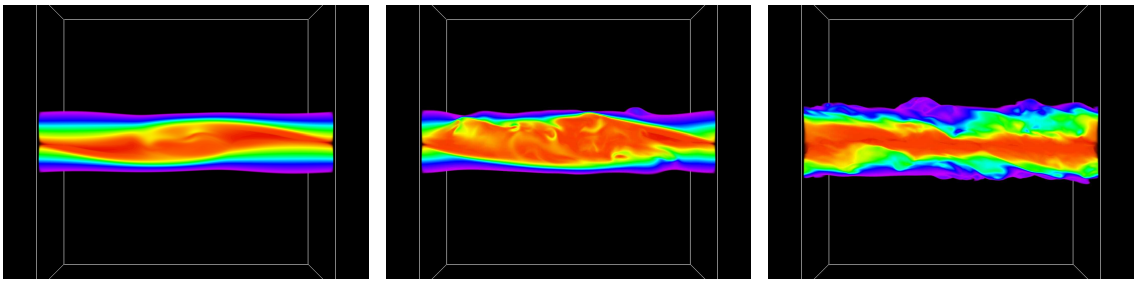

(a) time=55 (b) time=80 (c) time=105

FIGURE 8. Plots of kinetic energy for 3D DNS at three different snapshots in time.

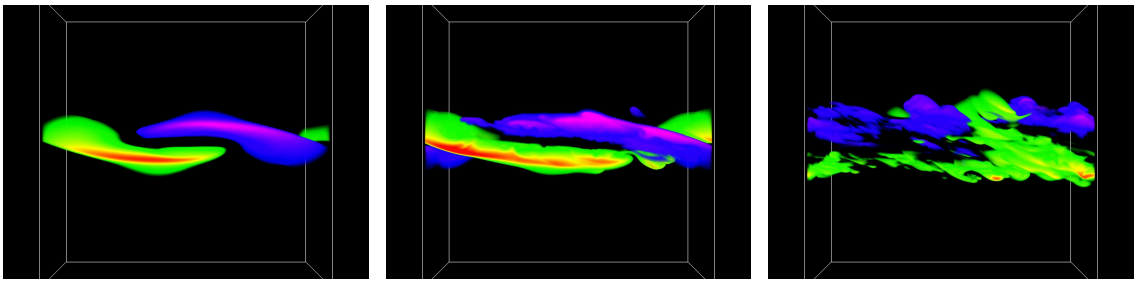

(a) time=55 (b) time=80 (c) time=105

FIGURE 9. Plots of temperature for 3D DNS at three different snapshots in time.

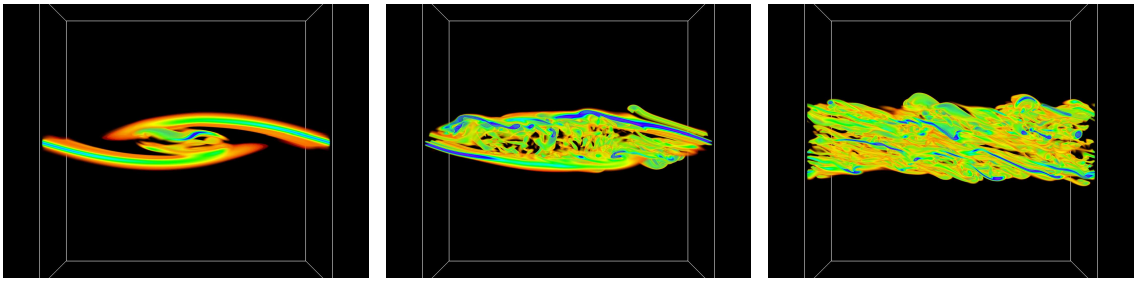

(a) time=55 (b) time=80 (c) time=105

FIGURE 10. Plots of the y component of vorticity for 3D DNS at three different snapshots in time.

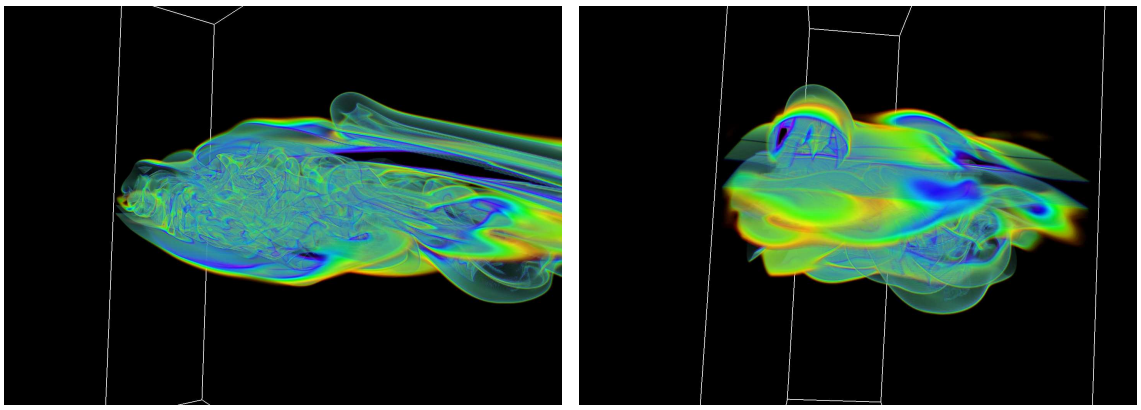

(a) angled view (b) longitudinal view

FIGURE 11. Enstrophy at peak energy showing the formation of a secondary instability.

4.2. **3D DNS.** The 3D DNS case is characterized by a lack of a billow structure and the rapid development of turbulence in the core of the instability. The evolution of enstrophy displayed in Figure 7 shows the core going turbulent at peak energy time. The turbulence then spreads outward preventing a development of an overturning billow. Figure 8 shows the kinetic energy remaining small near the center plane. Temperature is presented in Figure 9, which shows mixing occurring at late times. Figure 10 is the y-vorticity, which gives a good representation of the onset of turbulence. Small scale turbulence is quickly realized in the 3D DNS case, which prevents large scale overturning motions. Secondary roll instabilities do begin to form around peak kinetic energy time. Figure 11

displays enstrophy at peak energy time from new angles, which offers a good visualization of a roll structure developing outside the turbulent core.

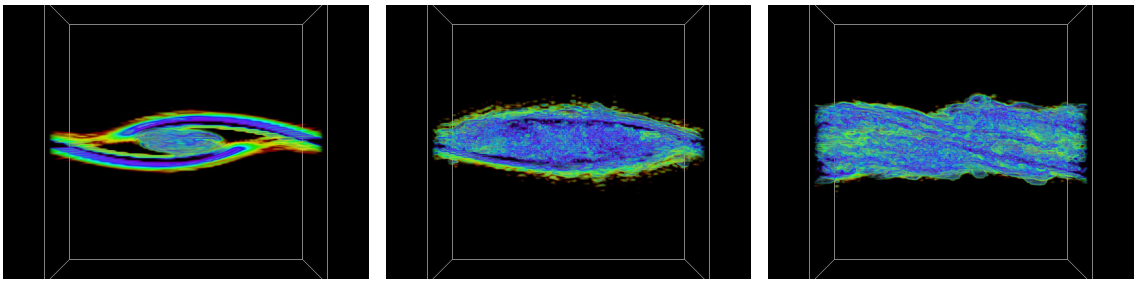

(a) time=55 (b) time=80 (c) time=105

FIGURE 12. Plots of enstrophy for 3D LES at three different snapshots in time.

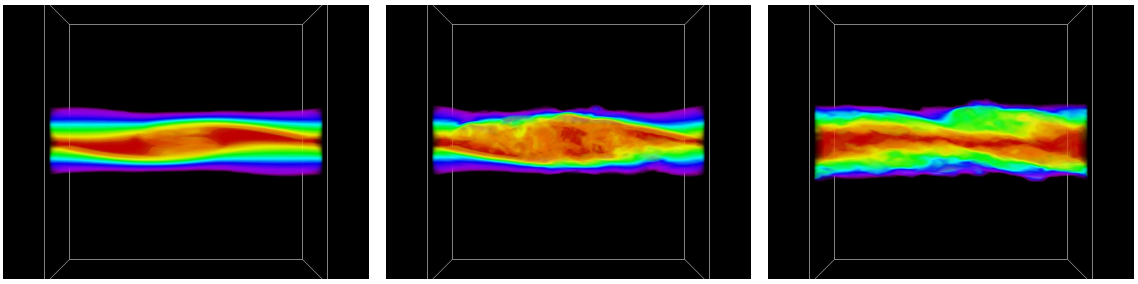

(a) time=55 (b) time=80 (c) time=105

FIGURE 13. Plots of kinetic energy for 3D LES at three different snapshots in time.

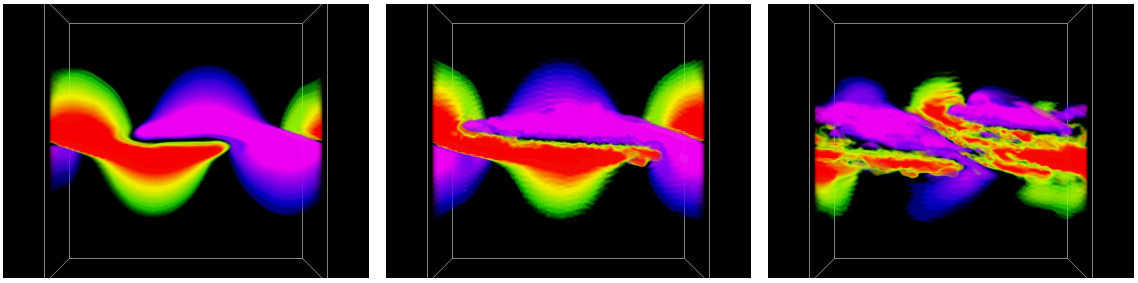

(a) time=55 (b) time=80 (c) time=105

FIGURE 14. Plots of temperature for 3D LES at three different snapshots in time.

4.3. **3D LES.** The 3D LES case gives similar qualitative results to that of the 3D DNS case. Therefore, the turbulent core at peak energy time is seen from the evolution of enstrophy displayed in Figure 12. The 3D LES results appear noisy with global oscillatory errors in derivative quantities such as enstrophy (the errors do not appear in velocity or temperature fields). This can be attributed to an unsatisfactory resolution for the 3D LES case. The kinetic energy in Figure 13 remains small near the center plane, while mixing is obvious from the temperature field in Figure 14. The turbulent core at peak energy time and the spreading of turbulence at late times is again apparent from the y-vorticity in Figure 15. The oscillatory error is also visible in this derivative quantity. The 3D LES case is characterized by a similar development of turbulence and structure as the 3D DNS case.

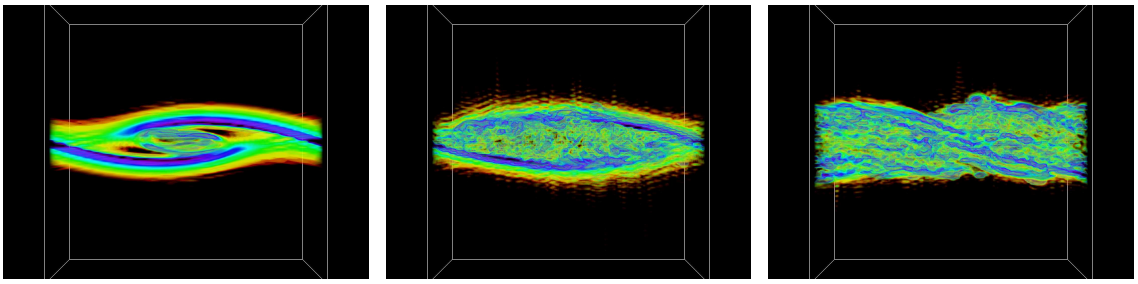

(a) time=55 (b) time=80 (c) time=105

FIGURE 15. Plots of the y component of vorticity for 3D LES at three different snapshots in time.

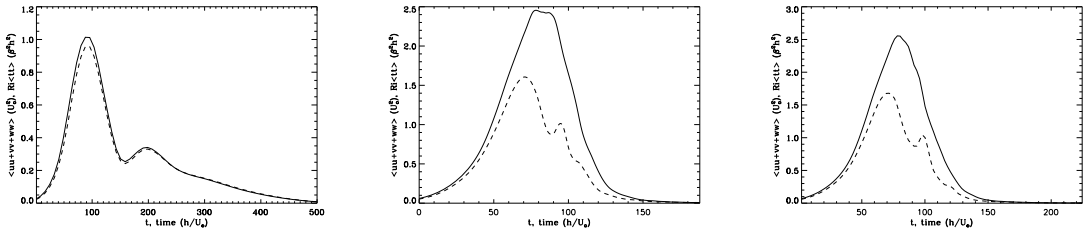

(a) 2D DNS (b) 3D DNS (c) 3D LES

FIGURE 16. Time plot of kinetic and potential energy for 2D DNS, 3D DNS, and 3D LES.

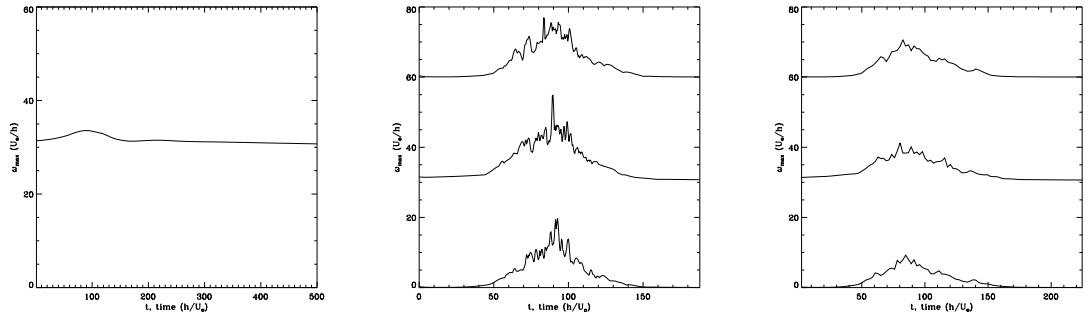

(a) 2D DNS (b) 3D DNS (c) 3D LES

FIGURE 17. Time plot of the maximum vorticity for 2D DNS, 3D DNS, and 3D LES.

4.4. **Comparison of 2D DNS, 3D DNS, and 3D LES.** It is clear from Figures 3 - 6, that the 2D simulation is fairly laminar compared to the 3D simulations shown in Figures 7 - 10. A comparison of the potential energy and kinetic energy versus time is shown in Figure 16. These plots show that energy peaks slightly later in the 2D DNS simulation, since there is no turbulent assisted mixing and two-dimensional structures naturally require larger time scales to develop and decay. The magnitude of the energies is also much less in 2D DNS, due to the absence of turbulence. Figure 17 shows a comparison of vorticity. The 2D case only has the y-component of vorticity. However, it is clear that the small scale features are not present in the 2D case.

The 3D DNS and LES results shown in Figures 12 - 15 and Figures 7 - 10 are very similar. A comparison in Figure 16 shows that the peak of energy and the magnitude of the energy for each are

close to identical. This supports the subgrid scale model used for the LES doing a successful job. For the Richardson number used in this project, small scale laminar structures are almost non-existent. Since almost all of the small scale structures are truly turbulent, the LES accurately models the part of the energy spectrum above the resolved physics. The plots of vorticity in Figure 17 vary due to the modeling of the small scales in LES. The sharp, jagged variations present in the DNS vorticity plot are due to resolving the small scales.

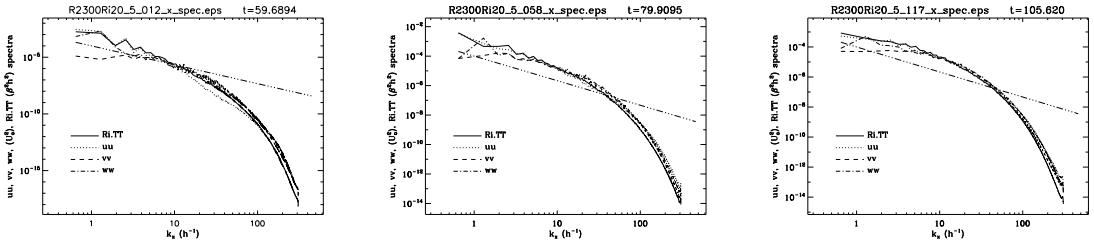

(a) time=55 (b) time=80 (c) time=105

FIGURE 18. Plots of x-direction spectra at three different snapshots in time. The diagonal line represents a -5/3 power dependence and is displayed for comparison.

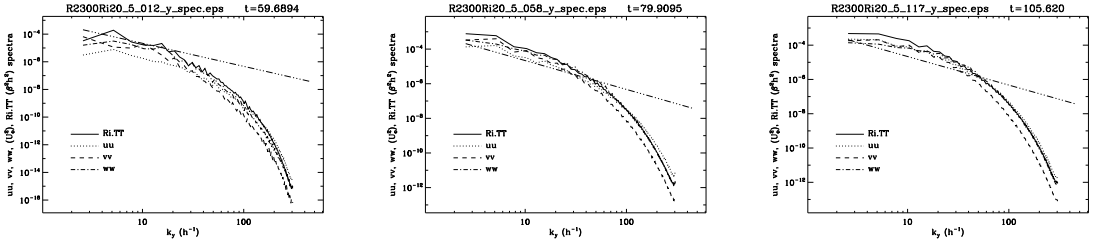

(a) time=55 (b) time=80 (c) time=105

FIGURE 19. Plots of y-direction spectra at three different snapshots in time. The diagonal line represents a -5/3 power dependence and is displayed for comparison.

4.5. **Energy Spectra.** The kinetic energy (as individual components) and squared temperature spectra are computed for the three time periods of interest using the 3D DNS results. The spectra are computed in a given direction on the midplane. The x-direction spectra are shown in Figure 18, whereas the y-direction is considered in Figure 19. Since the flow is in the x-direction, the spectra contains energy in lower wavenumbers for that direction. In all plots, the shape of the spectra for each quantity considered is fairly equivalent. At early times before the core has begun to show turbulent characteristics, an inertial range cannot be identified. However, near peak energy and at later times, an inertial range can be estimated by comparing the spectra to the -5/3 power relation line. The upper end of the inertial range is around a wavenumber of 20. Beyond the inertial range lies a large dissipation range, suggesting a steady cascade of energy to smaller scales in this fully turbulent system.

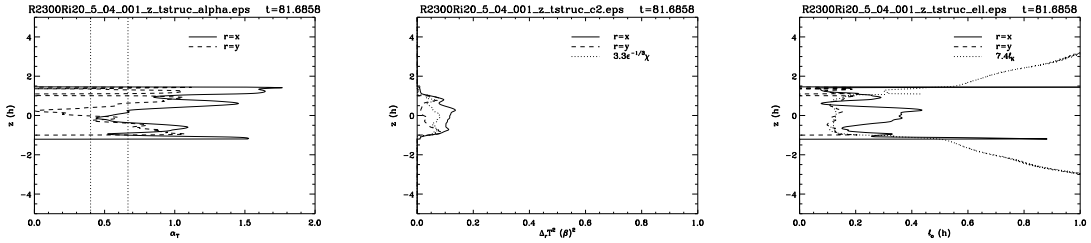

(a) α (b) C^2 (c) l

FIGURE 20. Second order structure function for temperature for α, C^2, and l and the time of peak energy.

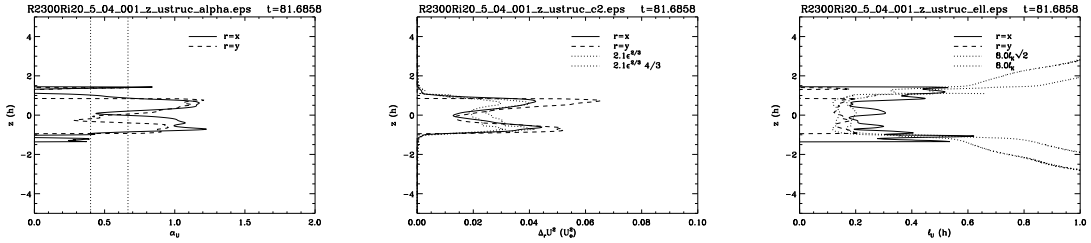

(a) α (b) C^2 (c) l

FIGURE 21. Second order structure function for velocity for α, C^2, and l and the time of peak energy.

4.6. **Second Order Structure Functions.** Additional analysis can be carried out through second-order structure functions. This analysis is done by computing two-point correlation functions of various flow fields. These correlations are then fit to a function form of

$$\Delta_r A^2 = Cr^\alpha,$$

where Δ_r is the correlation operator, A is the flow field (in this case T^2 or U^2), C is the amplitude of the correlation, r is the separation distance, and α is the power-law index. The parameter l corresponds the length scale at which the structure function is normalized. Study of turbulence models by Kolmogorov in 1941 and Bolgiano in 1959 suggest that α should have a value between $\frac{2}{5}$ and $\frac{2}{3}$. As one can see from Figure 20 and 21, our simulations are within this range in the central region around $z = 0$, but in the layers of high shear and outside the billows, the values are higher and much lower, respectively. The high values of correlation at $z = \pm 1.5$ are due to the large shear layers that flow in a nearly laminar configuration, yielding a high degree of order and structure to the flow. Inside the turbulent regions, our simulation data matches what is expected from turbulent theory much better. The lines referring to $r = x$ and $r = y$ are the planes in which the correlation function is computed. By comparing the strengths of the correlation in temperature and velocity, it is clear that there is much more structure in the temperature field. This suggests that the velocity varies on a much shorter scale.

4.7. **Vertical Profiles.** In order to further analyze the system, various contributing terms in the equations are horizontally averaged (in both x and y) and computed along the vertical direction. The vertical profiles for heat flux in all directions are shown in Figure 22. The heat flux in the system is almost completely in the x-direction. Furthermore, the heat flux is maximum at peak kinetic energy time, followed by small heat fluxes at late times. The heat flux is low near the center

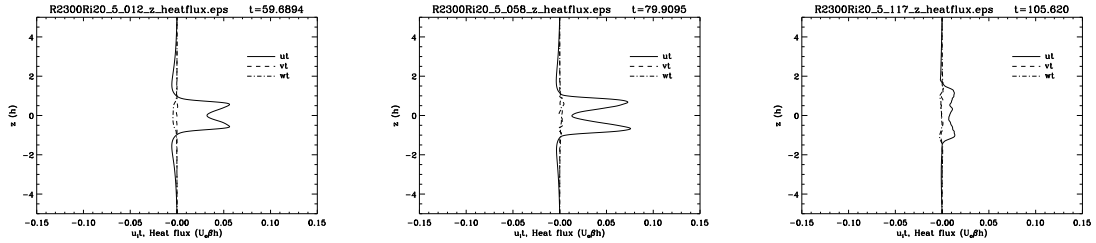

(a) time=55 (b) time=80 (c) time=105

FIGURE 22. Plots of heat flux at three different snapshots in time.

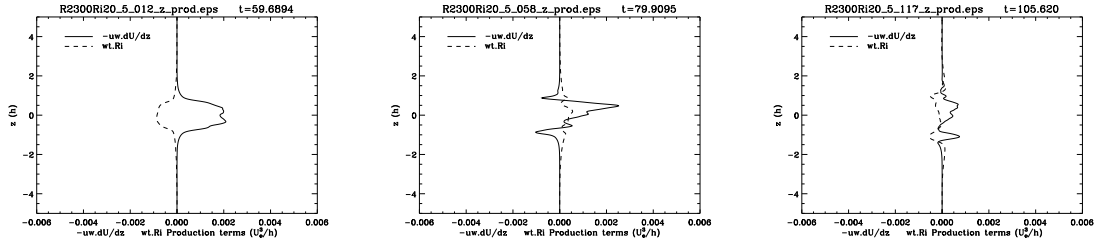

(a) time=55 (b) time=80 (c) time=105

FIGURE 23. Plots of production terms at three different snapshots in time.

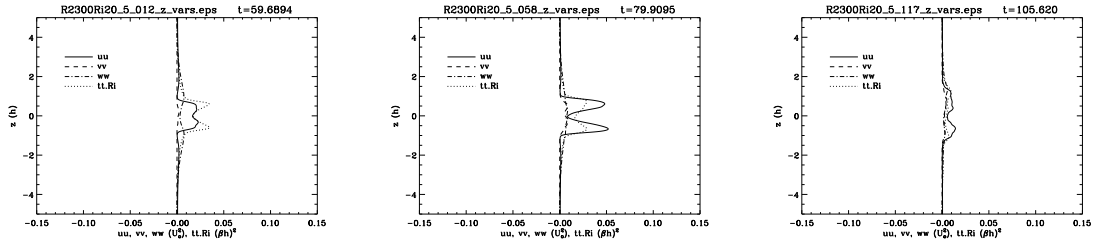

(a) time=55 (b) time=80 (c) time=105

FIGURE 24. Plots of all components of kinetic energy and variations of temperature squared at three different snapshots in time.

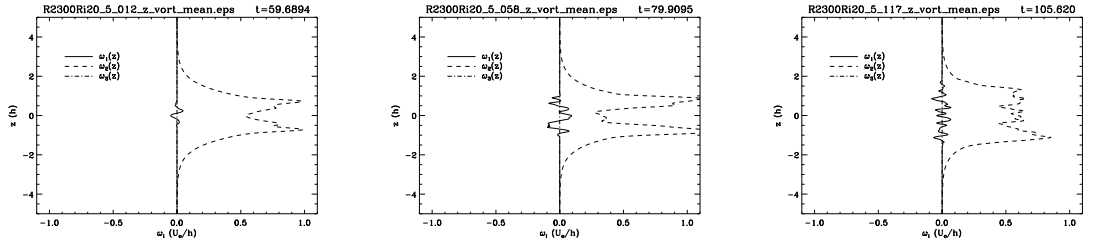

(a) time=55 (b) time=80 (c) time=105

FIGURE 25. Plots of mean vorticity at three different snapshots in time.

and symmetrically greatest away from the center. The vertical profiles of the production terms are given in Figure 23. These terms appear to contribute most prior to peak kinetic energy time. At late times, when turbulence dominates the flow, the production terms contribute relatively small amounts. The vertical profiles for all components of squared velocity and squared temperature are shown in Figure 24. The x-direction again dominates the motion of the system. That is, v^2 and w^2 are negligible when compared to the contribution from u^2. The squared temperature is of similar order and shape to u^2. The maximum for these quantities occur around peak kinetic energy time and are symmetric about the center plane with low values on the center plane. At late times, all quantities have been reduced due to the the turbulent decay of the instability toward a stable system. The vertical profiles for the mean of all components of vorticity are shown in Figure 25. The y-direction vorticity dominates these plots since the primary rotation occurs in the $x - z$ plane. It reaches its maximum at peak energy time. At late times, relatively high amounts of vorticity are retained as the energy is continual dissipated at the smallest scales. The x-direction vorticity shows slight variations, whereas the z-direction vorticity remains close to zero due to the horizontal averaging. Mean velocity and temperature profiles are computed but not displayed since the variation with time for these quantities is unobservable.

4.8. **Richardson Number Dependence.** The work done for this study is part of a threefold attack at the Kelvin-Helmholtz instability problem. Two other groups tackled lower Richardson number cases, particularly $Ri = 0.05$ and $Ri = 0.1$. Whereas the $Ri = 0.2$ case considered in this study results in a quickly developing turbulent core followed by a rapid instability decay, leading inevitably back to a stable system, the lower Richardson number cases yield much different physics. The most extreme case of $Ri = 0.05$ results in a persistent billow structure that has a chance to rotate before becoming turbulent. The rotation continues even after the turbulent transition, which leads to a rather large inertial range in the spectra for the longitudinal direction. The peak kinetic energy occurs around $t = 30$, which is much earlier than the $Ri = 0.2$ case. Furthermore, the decay in kinetic energy and turbulence as seen in this project is not observed in the low Ri case. Since the large scale billow persists over long periods of time, small scale laminar motions are introduced. This causes LES to perform poorly on the system. The intermediate case of $Ri = 0.1$ is characterized by the development of a billow with a small rotating core, which rotates about once before blossoming into turbulence. The size of the inertial range observed in the kinetic energy spectra is also an intermediate value between the two extreme Ri cases. Fine grained vortex tubes are observed during the turbulent stages for this case. LES does slightly better for this case, but it still has its problems handling the laminar motion in the subgrid scales. At the limiting case of $Ri = 0.25$, theory says that the system is stable. For $Ri = 0.2$, as studied in this project, slight variations in the effective mean shear or buoyancy lead to variations in the effective Richardson number. Therefore, the lack of a strong billow structure along with the whole layer developing turbulence may be acting to modify the effective shear of the system forcing it toward stability.

5. Conclusion

This study was successful in investigating the $Ri = 0.2$ case, where the core of the instability goes turbulent quickly. This is followed by a rapid spreading outward leading to the entire layer filling with turbulence without any large scale overturning motion. Two dimensional simulations of this system are unreliable since turbulence is intrinsically a three dimensional process. The system remains laminar for the 2D case. For higher Richardson numbers ($Ri > 0.2$), LES does a great job of capturing all the physics of the flow while only requiring a fraction of the necessary resolution for a DNS run. However, at lower Ri, LES cannot model laminar behavior at small scales introduced from the overturning billow. The analysis of the energy spectra for this system supports the development of turbulence and the cascade of energy to smaller and smaller scales. As the instability grows and decays, the system becomes more dissipative. The growth and sustainability of the Kelvin-Helmholtz instability is heavily dependent upon the parameters, specifically the Richardson number. For $Ri > 0.25$, the system remains stable. However, for Ri slightly smaller than this threshold, the instability is shown to develop and decay rapidly, going through a fully turbulent stage along the

way. As the Richardson number drops further, the large structures of the flow tend to persist before the development of a fully turbulent layer. For a far-off observer looking to take a pretty picture of the billowing clouds, one hopes for a low Richardson number configuration. However, for those in the airplane flying through the shearing air, the higher the Richardson number, the better (preferably above 0.25).

References

1. J. Clyne, P. Mininni, A. Norton, and M. Rast, *Interactive desktop analysis of high resolution simulations: application to turbulent plume dynamics and current sheet formation*, New Journal of Physics **9** (2007), 301–+.
2. M. Rast and J. Clyne, *Coupled Analysis and Visualization of High Resolution Astrophysical Simulations*, Numerical Modeling of Space Plasma Flows (N. V. Pogorelov, E. Audit, and G. P. Zank, eds.), Astronomical Society of the Pacific Conference Series, vol. 385, April 2008, pp. 299–+.
3. J. F. Scinocca, *The mixing of mass and momentum by kelvin-helmholtz billows*, American Meteorological Society (1995).

Department of Mechanical Engineering† and Department of Astrophysics§, University of Colorado at Boulder

E-mail address: samuel.skillman@colorado.edu, scott.reckinger@colorado.edu, shanon.reckinger@colorado.edu